




Experimental Technique to Generate Complex Pressure Cycles in TBI-related In-vitro or Ex-vivo Samples

S. Vidhate¹ · A.M. Willis^{2,3} · R. Mejia-Alvarez¹ 

Received: 7 April 2020 / Accepted: 20 February 2021 / Published online: 25 March 2021
© The Society for Experimental Mechanics, Inc 2021

Abstract

Blast-induced traumatic brain injury (bTBI) has been widely accepted as a “signature” wound affecting service members in modern conflicts, yet the mechanisms that cause bTBI still remain poorly understood. One of the main reasons for such poor understanding is the technical challenge of reproducing under controlled laboratory conditions the typical time-varying loading cycles induced on brain tissue after a blast event. Blast events have a sub-millisecond onset of high pressure followed by complex dynamics resulting from interaction between the blast wave and the complex anatomical structure of the human head. To tackle these experimental challenges, our group developed a novel apparatus using a water-filled piston-cylinder assembly driven by a piezoelectric actuator to generate complex and fast-varying pressure profiles. The versatility of our apparatus in producing complex pressure profiles was demonstrated by generating a single pressure pulse with various pulse-widths and magnitudes, an approximate Friedlander waveform, and a multi-modal waveform. A feedforward controller was also designed for the apparatus enhancing its capabilities to generate custom, user-defined pressure profiles. The apparatus successfully generated pressures up to 450 kPa at frequencies up to 5 kHz. The designed apparatus is compact, easily portable, and highly controllable, making it well suited for biomedical applications. This apparatus can be used to conduct *ex-vivo* and *in-vitro* experiments involving animal brain tissue specimens, cell cultures, and organoids to explore their response to the complex pressure loadings observed during a bTBI event.

Keywords Blast-induced traumatic brain injury · Piezoelectric actuator · Complex pressure profiles · Blast loading · Feedforward controller

Introduction

Blast-induced traumatic brain injury is one of the major health issues affecting soldiers in the battlefield. It has been a leading cause of mortality and disability sustained by armed forces and law enforcement personnel. The statistics regarding casualties in U.S. military operations held in Iraq and Afghanistan reported 253,300 traumatic brain injury cases between 2000 and 2012 with over 75% of the cases linked to mild-TBI [1]. Additionally, this issue has caused

a financial burden of billions of dollars to the health care system [2].

As stated in [3–5], injuries associated with blast exposure follow four distinct categories: *primary* injuries are caused by the interaction of the blast wave directly with the brain tissue leading to a mechanical damage; *secondary* injuries result from projectile (shrapnel) penetration into the head; *tertiary* injuries are caused by blunt impacts as a result of being propelled away by the explosion; and *quaternary* injuries include other forms of injury such as polytrauma, thermal, and chemical burns [6, 7]. Of all these, *primary* injuries are the least understood and, thus, have been the main focus of our research. Primary blast injuries are hypothesized to be linked with diffuse axonal injury, vascular tears, intracranial hemorrhage, and focal cortical contusion [8]. Though brain soft-tissue damage resulting from shear [9, 10], cavitation [10–12], traumatic cell deaths, and disrupted cell structures [13, 14] have been identified as possible injury mechanisms involved in bTBI, the exact mechanisms associated with primary blast

✉ R. Mejia-Alvarez
rimejal@egr.msu.edu

¹ Department of Mechanical Engineering, Michigan State University, East Lansing, MI 48824, USA

² Department of Neurology, Brooke Army Medical Center, Fort Sam Houston, TX 78234, USA

³ Department of Neurology and Neurotherapeutics, University of Texas Southwestern, Dallas, TX 75390, USA



exposure and their neuropathological consequences still remain ambiguous.

One of the major contributing factors for such ambiguity is the difficulty in replicating intracranial pressure (ICP) profiles observed during a blast exposure to induce mechanical insults within brain tissue specimens or cell cultures. The blast-wave generated from an improvised explosive device (IED) explosion follows the characteristics of a Friedlander waveform [15, 16]. When this blast wave interacts with the skull and the intricate anatomical structure inside the head, it generates complex and highly dynamic ICP profiles [17, 18]. These complex ICP profiles are a result of transmissions and reflections of the incident wave from the multi-material structure of the head [19]. Unsteady deformation of the skull also contributes to the complexity of the ICP profiles [19–21]. In order to fully understand the underlined pathological effect of mechanical insults from complex ICP profiles on brain tissue specimens or cell cultures, there is a need for an experimental apparatus that can generate such pressure profiles under laboratory conditions.

Previously, researchers have implemented experimental techniques such as split-Hopkinson pressure bars (SHPB) [13, 14, 22, 23], shock-tubes [24–30], and blast-tubes [31–34] to generate pressure profiles mimicking a blast loading. In the SHPB technique, a traveling stress wave is generated in the incident bar from a striker impact. This wave is then used to compress water and generate impulsive pressures in the piston-cylinder assembly placed at the end of the bar. Shock-tubes use a sudden release of compressed gases to generate impulsive pressures. And blast-tubes use confined explosive detonations to generate impulsive pressures. These experimental setups generate pressure profiles that have a single overpressure pulse either sustained or similar to a Friedlander. Other researchers have used microdetonics to generate blast loading [35, 36]. All of the above-mentioned techniques have a limited control over the pressure profiles that they can generate, are not easily tunable to replicate the ICP dynamics, and are in general very expensive, requiring significant technical expertise and large laboratory spaces.

An ideal solution to these experimental challenges would be to create a completely controllable, portable, reproducible, and inexpensive method to generate arbitrarily complex pressure cycles onto living tissue and cell cultures. Building an apparatus that is easily shared between laboratories would also accelerate bTBI research. Our study demonstrates the design and control of such a novel experimental apparatus that can generate tunable, reproducible, and complex pressure loading cycles.

This paper is organized as follows. Section “**Design**” discusses the working principle and the fabricated design of the apparatus. A simplistic numerical model analyzing the

apparatus is also discussed in this section. Section “**Control**” discusses the system identification methodology used to characterize the input-output relation of the apparatus. A feedforward controller designed based on the system identification data to generate user-defined pressure profiles is also detailed in this section. The results from experiments conducted to generate various pressure profiles using the apparatus are discussed in “**Results and Discussion**” section. Lastly, “**Conclusion**” section concludes the discussion on the experimental apparatus.

Design

Working Principle

Pressure is a surface loading that compresses a specimen from all directions. In this study, a piston-cylinder assembly filled with water (Fig. 1) was used as a variable-volume confinement for generating pressure loading. Water is considered a nearly incompressible fluid because of its very high bulk modulus of 2.15 GPa [37]; hence, its pressure rises sharply as a response to relatively small volume changes.

The change in pressure inside the cylinder, ΔP , can be estimated using the Hooke’s law for volumetric loading [38, 39] given by the equation

$$\Delta P = -K \frac{\Delta V}{V_0}, \quad (1)$$

where K is the bulk modulus for water, V_0 is the initial volume of water inside the cylinder, and ΔV denotes the change in volume of water. Assuming the cylinder walls to be perfectly rigid and the cylinder having a uniform cross-section, equation (1) can be further simplified to

$$\Delta P = K \frac{u_p}{l_0}. \quad (2)$$

Here, l_0 and u_p denote the initial length of the water volume inside the cylinder and the displacement of the

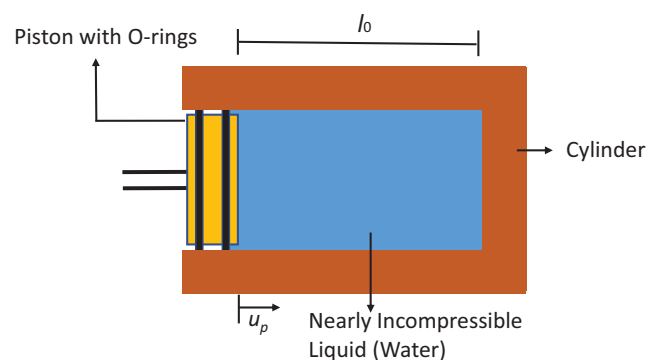


Fig. 1 A piston-cylinder assembly. l_0 : initial length of the water volume inside the cylinder. u_p : displacement of the piston

piston respectively as shown in Fig. 1. As the bulk modulus of water is extremely high, even a piston displacement of a few micrometers can generate a high pressure spike inside the cylinder, equivalent to a blast event. A piezoelectric stack actuator (Model P885.95 Physik Instrumente (PI) GmbH & Co. KG, Karlsruhe, Germany) was used to drive the piston in the piston-cylinder assembly as shown in Fig. 2(a). The piezoelectric actuator expands when a voltage signal is applied across its leads. By expanding, the actuator displaces the piston, compressing the water inside the cylinder and rising the pressure as a result. The time scale of this actuation is of the order of a few microseconds; this is fast enough to generate pressure loadings similar to those of a blast event (typically lasting for a few milliseconds). A high-frequency pressure transducer (Model 113B27 PCB Piezotronics Inc., Depew, NY, USA) measures the pressure inside the cylinder to give feedback about the actual performance of the piezoelectric actuator.

Device Fabrication

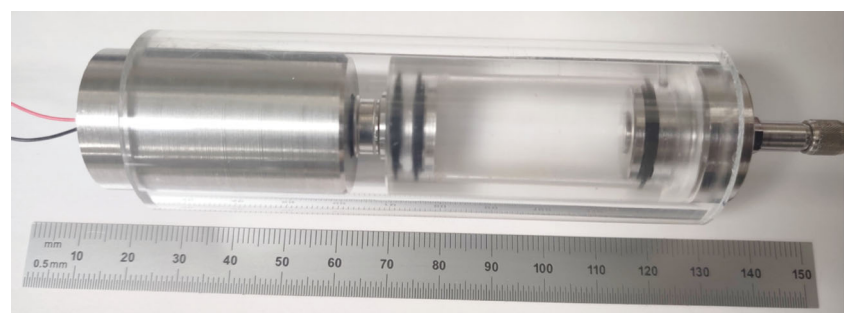
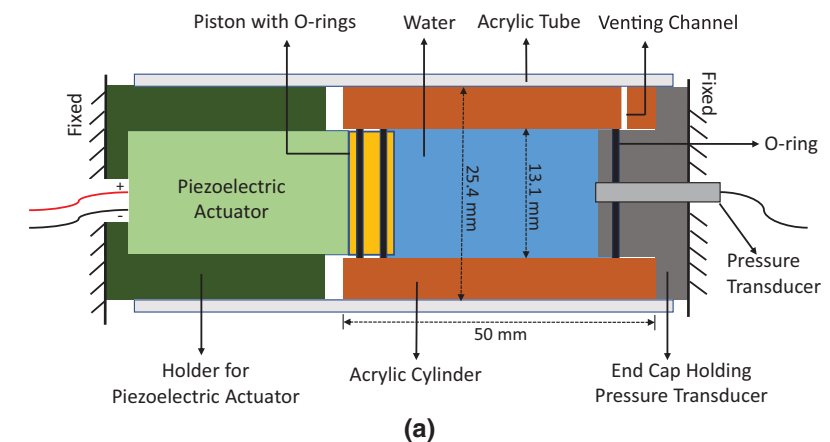
The pressure chamber was machined from an acrylic rod (25.4 mm diameter) by drilling a through-hole of 13.1 mm diameter. A custom end-cap was designed and machined from a medical-grade SAE 316L stainless-steel rod (25.4 mm diameter) to hold the pressure transducer as

well as seal one end of the chamber. The other end of the chamber was sealed using a stainless steel piston with O-rings. A venting channel, that is a 1.6 mm diameter hole drilled perpendicular to the pressure chamber axis, was incorporated in the pressure chamber to remove air bubbles and excess water while filling the chamber. The design of the venting channel is similar to the one implemented in [12]. A custom stainless steel holder was machined to house the piezoelectric actuator. An acrylic tube (ID 25.4 mm and OD 31.75 mm) was used to align the pressure chamber and the actuator. The schematic and the fabricated design of the apparatus are shown in Fig. 2(a) and 2(b) respectively. A block with a V-shaped groove to support and align the actuator/chamber system was designed and 3D-printed out of polylactic acid (PLA) filament. The assembly was held together using a fixture built from aluminum plates and steel threaded rods as shown in Fig. 3(a). This fixture was also used to pre-compress the assembly to remove any slack that would prevent effective compression. The complete setup of the apparatus including the fixture is shown in Fig. 3(b).

Instrumentation

The input to the apparatus was a 0–10 V signal. This input signal was amplified to 0–100 V using a power amplifier (Model E504 Physik Instrumente (PI) GmbH & Co.) and then fed to the piezoelectric actuator. The input voltage

Fig. 2 (a) Cross-sectional schematic view and (b) Fabricated design of the experimental apparatus (150 mm ruler placed for size reference)



(b)

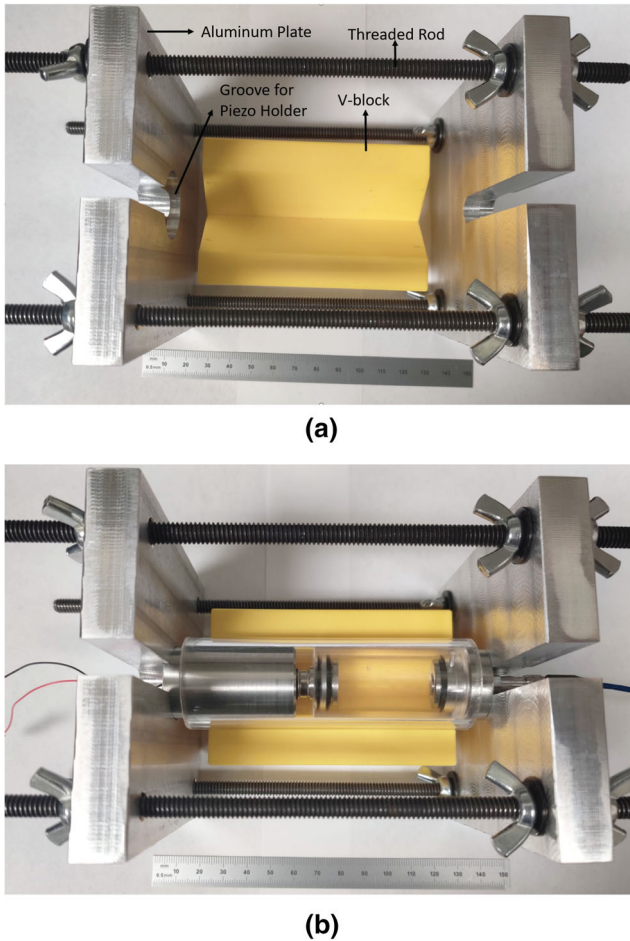


Fig. 3 (a) Apparatus fixture consisting of aluminum plates and steel threaded rods along with the supporting V-block (b) Completed assembly of the experimental apparatus

signal determined the displacement of the piston and altered the pressure in the chamber, which was measured using the pressure transducer. A signal conditioner (Model 482A21 PCB Piezotronics, Inc.) was used to amplify the pressure signal measured by the transducer, which was finally recorded using a data acquisition device (Model USB-6341 National Instruments, Austin, TX, USA). The same data acquisition device was also used to generate the input voltage signal. A custom LabVIEW (National Instruments) program was developed to perform and synchronize both the signal generation and the data acquisition tasks at the sampling frequency of 100k samples per second.

Numerical Model

A numerical model of the apparatus was developed to further analyze the pressure generation mechanism and estimate the theoretical limit of maximum pressure that could be achieved. The pressure chamber, along with the piston and the end-cap, was modeled as a one-dimensional

domain as shown in Fig. 4. This assembly was simulated by solving the one-dimensional wave propagation equation,

$$\frac{\partial^2 u}{\partial t^2} = \alpha^2 \frac{\partial^2 u}{\partial x^2}, \quad (3)$$

which has one dependent variable u and two independent variables t and x [40]. For a longitudinal stress wave traveling through an elastic medium, u denotes the displacement at location x and time t . The constant α in equation (3) denotes the speed of the longitudinal stress wave traveling in the elastic medium. This wave speed was determined from the elastic modulus (E) and the density (ρ) of the elastic material using the relation

$$\alpha = \sqrt{\frac{E}{\rho}}. \quad (4)$$

Water was modeled as a linear elastic fluid [38]; and since it was fully confined, its bulk modulus was used as the elastic modulus. The steel parts were modeled as linear elastic solids [39]; and since they experienced uniaxial loading, Young's modulus was used as the elastic modulus for steel. The material properties (elastic moduli and densities) used for water and steel are given in Table 1. The acoustic impedance (Z) for the wave propagation in each medium was calculated using the relation

$$Z = \alpha \times \rho. \quad (5)$$

The interfaces between water and steel were modeled as bonded interfaces sharing common nodes. The stress wave interaction at the interface was modeled using the equations

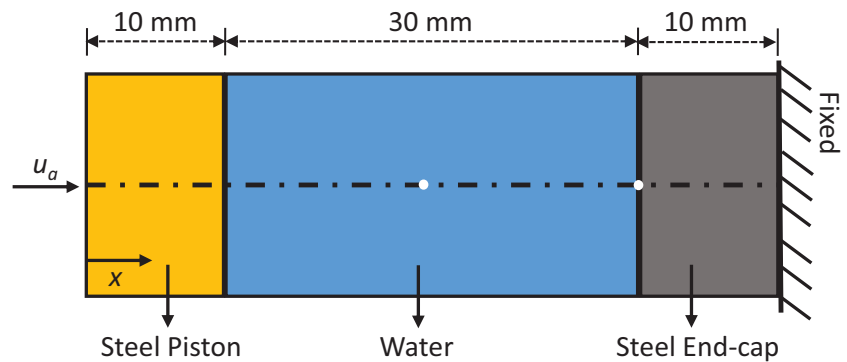
$$\sigma_r = \frac{Z_B - Z_A}{Z_B + Z_A} \sigma_i \quad (6)$$

$$\sigma_t = \frac{2Z_B}{Z_B + Z_A} \sigma_i, \quad (7)$$

where σ_i denotes the incident stress wave traveling through material A, which gets reflected from the interface as σ_r and transmits into material B as σ_t [41–43].

Displacement $u_a(t)$ was specified as a boundary condition at the left end of the piston (Fig. 4). This boundary condition physically represents the displacement provided by the piezoelectric actuator. A fixed boundary condition was specified at the right end of the end-cap (Fig. 4) to model the support by the aluminum plates and threaded rods fixture. The method of characteristics was implemented using a MATLAB (MathWorks Inc., Natick, MA, USA) script to numerically solve the one-dimensional wave propagation equation (equation (3)) for each of these media [40].

Fig. 4 One-dimensional domain for the numerical model simulating the pressure chamber with white dots showing the locations of the nodes used for extracting pressure profiles



As a test case, a sinusoidal profile having $7\ \mu\text{m}$ amplitude and 2000 Hz frequency was specified as a displacement boundary condition. This boundary condition mimics the displacement provided by the piezoelectric actuator at 2000 Hz operating frequency. The apparatus was simulated by numerically solving the governing equations and the pressure profiles were extracted for two locations of interest: first being the midpoint of the pressure chamber and second was the location where the pressure transducer was incorporated in the experimental setup. Figure 5 shows both the input displacement profile specified as the boundary condition and the pressure profiles extracted for the specified locations.

It is noticeable that the pressure profiles have the same form as the actuator displacement profile. Moreover, the two pressure profiles are almost coinciding, suggesting a minimal variation in the pressure across different locations inside the chamber. This observation supports the simplification of a hydrostatic pressure distribution inside the chamber as the piston speed is several orders of magnitude smaller than the longitudinal wave speed in water. Thus, the pressure generation can be directly linked to the piston displacement as stated in equation (2).

This model of the pressure chamber is a simplistic model that doesn't account for the components with non-linear response such as deformation of the o-rings and the chamber, friction between the o-rings and the pressure chamber walls, etc. Still, it is helpful in estimating the shape and the maximum expected magnitude of the generated pressure profiles. The effect of unaccounted components in the numerical model on the performance of the apparatus was further experimentally evaluated through

system identification, and a control strategy was developed to generate complex pressure profiles.

Control

To generate a user-defined, arbitrarily complex pressure loading cycle in a consistent and reproducible manner, a controller is needed for the pressure apparatus. Based on the user-specified target pressure profile, the controller needs to compute appropriate control input, i.e., an excitation voltage profile driving the piezoelectric actuator, such that the pressure profile generated by the apparatus closely follows the target pressure profile. In control theory, this control problem is termed as “output tracking problem” [44]. To design such a controller for the apparatus, first, the apparatus was characterized by correlating the inputs given to the apparatus and the measured outputs. This performance characterization is known as “system identification”, and is detailed in “[System Identification](#)”. MATLAB was used to generate the input signal, and to process the output data measured from the device. The results of processing this experimental data were used to develop a *feedforward* control that is detailed in “[Feedforward Control](#)”.

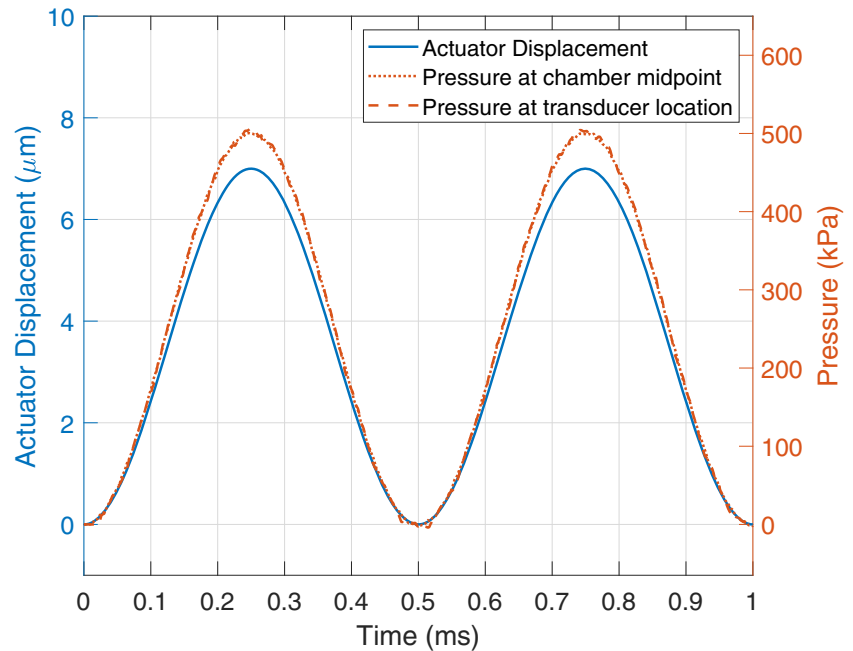
System Identification

The pressure apparatus is a single-input, single-output (SISO) system. The input to the system is an excitation voltage signal provided to the power amplifier driving the piezoelectric actuator. The output of the system is the pressure profile generated by the apparatus in response to the actuation of the piezoelectric actuator. For system identification, the response of the apparatus to various sinusoidal excitations was measured. A chirp signal, i.e., a constant amplitude sinusoid with continuously varying frequency, was given as input to the system to evaluate its frequency response. As an illustration, a chirp signal is shown in Fig. 6. This chirp signal has a starting frequency

Table 1 Material properties for the numerical model

Material	Elastic modulus (GPa)	Density (kg/m^3)
Water	2.15 (Bulk Modulus)	998
Steel	200 (Young's Modulus)	7850

Fig. 5 Comparison between the actuator displacement profile (left y-axis) specified as the input boundary condition to the numerical model and the output pressure profiles (right y-axis) obtained from the numerical simulation



f_o and end frequency f_T , and the instantaneous frequency f is linearly increased from f_o to f_T over the total duration of the signal (T) as given in equation

$$f(t) = f_o + \left(\frac{f_T - f_o}{T}\right) \times t. \quad (8)$$

The *chirp* function in MATLAB was used to generate this signal profile.

To evaluate the frequency response of the system, the system was excited with chirp input signals having $f_o = 100$ Hz and $f_T = 5$ kHz for a total duration of 100 ms. This frequency range was specifically chosen as the dominant frequencies in the ICP profiles observed in a bTBI event fall within this range [17, 18]. Multiple experiments were performed to evaluate the system's response to such chirp inputs of various magnitudes. For each of the chirp signal, an offset equal to the amplitude of the sinusoids was added to make the chirp signal non-negative. The input parameters for these sine-sweep experiments are given in Table 2.

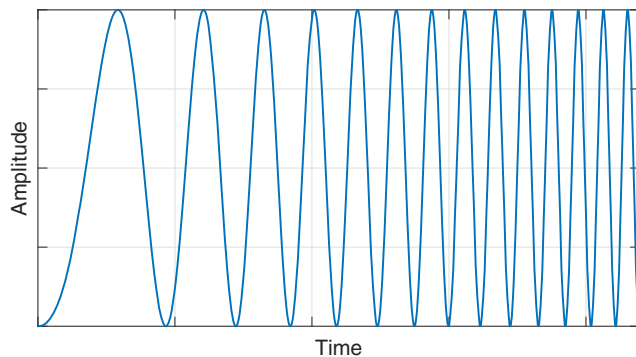


Fig. 6 A chirp signal

As a representative result, the chirp input signal having 6 V amplitude is shown in Fig. 7(a), and the corresponding output pressure profile generated by the apparatus is shown in Fig. 7(b). There was a transport delay between the input excitation and the pressure output profiles, which corresponds to the response time of the system. This transport delay was measured using the correlation-based *finddelay* function in MATLAB and was found to be 80 μ s. This transport delay was removed from further analysis by defining a new start time for the pressure output profile. It can be observed that even though the input signal had a fairly constant amplitude for all the excitation frequencies, the output pressure profile exhibits amplitude variation with input frequencies. This amplitude variation of the sinusoids constituting the input and the output profiles was quantified by analyzing the profiles in the frequency domain.

The amplitude variation was characterized by computing the gain, i.e., the ratio of output amplitude to input amplitude for a particular frequency. The DC gain was also determined by computing the ratio between the output and input amplitudes for the zero frequency. Additionally, the phase difference between the sinusoids constituting the input and the output profiles was computed from the frequency-domain data. The gains and the phase differences for the sinusoids were determined for all the system identification experiments. These gains and the phase differences computed from the input-output data for each of the 10 experiments are shown in Fig. 8(a) and 8(b) respectively.

The gain and the phase difference curves determined from the experimental data are consistent over all the experiments. The gain curves clearly capture the local



Table 2 Input parameters of the sine-sweep system identification experiments

Start frequency (Hz)	End frequency (kHz)	Duration (ms)	Input amplitude (V)	Number of experiments
100	5	100	2	2
100	5	100	4	2
100	5	100	6	2
100	5	100	8	2
100	5	100	10	2

resonances present in the system even though the exact factors causing the resonances are hard to isolate or predict analytically. The average gain and the average phase difference curve are also shown in the above Fig. 8(a) and 8(b). Thus, by using these average gain and the average phase difference curves, the system output can be predicted for a sinusoidal input having a frequency between 100 Hz to 5 kHz.

By knowing how the amplitudes and phases of sinusoids change from input to output and modeling the system as a linear time-invariant system [45], the response of the system

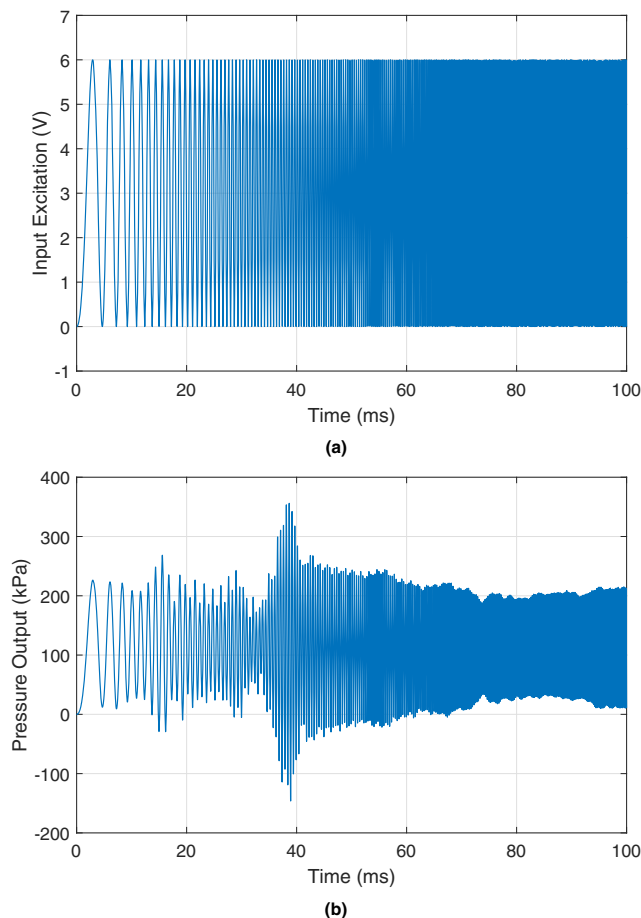


Fig. 7 (a) Chirp voltage profile given as an input to the pressure apparatus for a system identification experiment (b) Output pressure profile generated as a response to the chirp excitation

can be predicted for an arbitrarily complex input profile composed of the sinusoids of these frequencies. Finally, the system identification curves, the average gain curve and the average phase difference curve, were used to design a feedforward controller for the output tracking problem.

Feedforward Control

For the output tracking problem, the target output profile to be tracked is provided as an input to the controller. A feedforward controller was designed to compute a control input profile such that the output generated by the system tracks the target output profile. The feedforward controller used the system identification curves, the average gain curve and the average phase difference curve, to compute the control input profile.

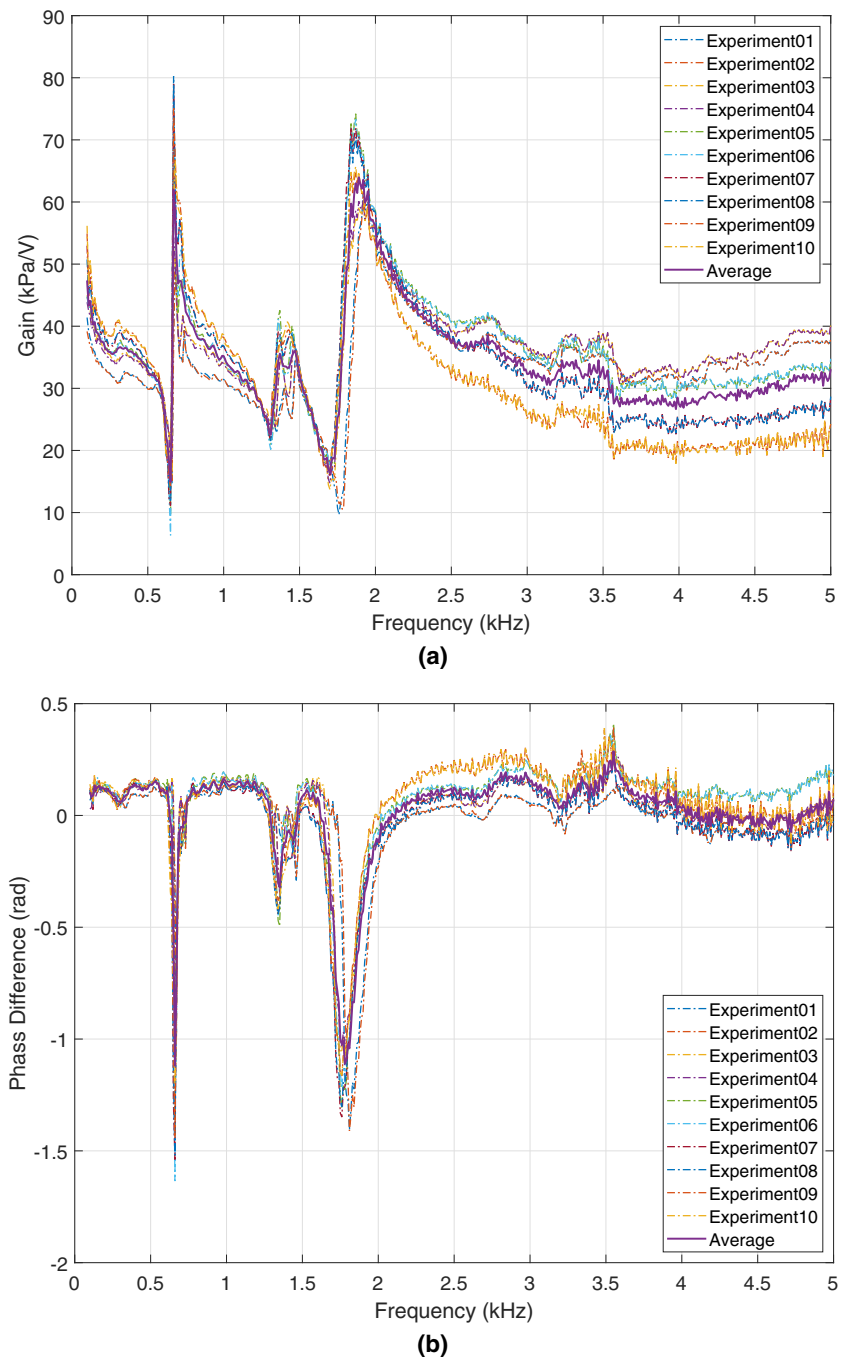
First, the target output profile was transformed into its frequency-domain representation to determine the amplitudes and the phases of the sinusoids of which it is composed. Then, the amplitudes of the sinusoids for the control input signal were determined by dividing the output amplitudes with corresponding gains. Also, the phases of the sinusoids for the control input signal were calculated by incorporating the phase shift from the average phase difference curve into the phases of corresponding sinusoids in the target output profile. Once the amplitudes and phases of the sinusoids were determined for the control input signal, its time-domain representation was reconstructed. This control input signal was then provided to the system and the actual experimental output profile was measured. Lastly, the target output profile and the experimental output profile were compared to evaluate the performance of the feedforward controller. The implementation and the performance of this controller were tested by tracking a multi-modal pressure profile as detailed in “Multi-modal Waveform”.

Results and Discussion

To assess the capabilities and the performance of the apparatus, we designed a series of experiments to generate various



Fig. 8 (a) Gain curves and (b) phase difference curves determined from system identification experiments



pressure waveforms. Initially, we test the capability of the device to generate two simple waveforms without using the feedforward control. We demonstrate a single pulse waveform in “[Single Pulse Waveform](#)”, and an approximate Friedlander waveform in “[Friedlander Waveform](#)”. Subsequently, we demonstrate the implementation of the feedforward control to generate a multi-modal waveform in “[Multi-modal Waveform](#)”.

Single Pulse Waveform

In order to generate a single pressure pulse, a single sinusoidal voltage pulse was given as an input to the apparatus. Three such voltage excitation pulses having different pulse widths and amplitudes were constructed as detailed in Table 3. The excitation voltage vs time graph for these pulses is shown in Fig. 9(a). The corresponding

Table 3 Input excitation pulses constructed for generating pressure pulses

Excitation Pulse No.	Pulse width (ms)	Pulse amplitude (V)
1	0.50	8
2	1.75	10
3	6.00	7

pressure pulses generated as a result of these input voltage pulses are shown in Fig. 9(b).

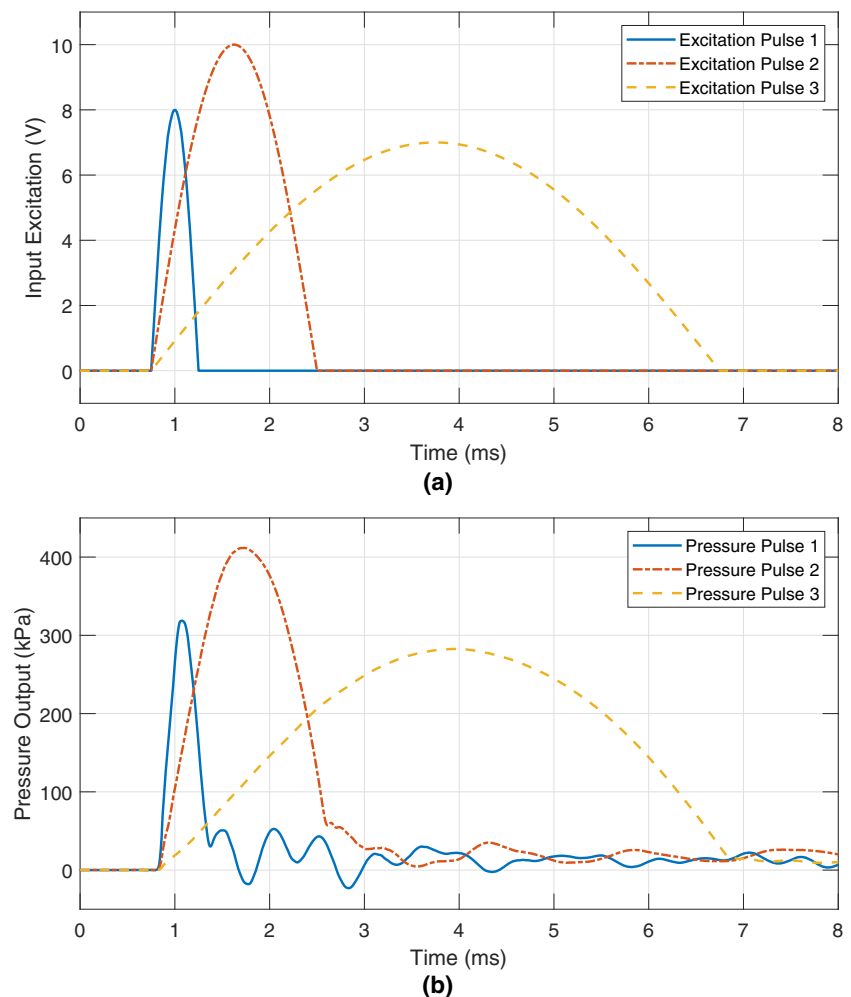
It can be observed that the pressure pulses closely follow the temporal and magnitude characteristics of the input voltage pulse. Thus, by changing pulse widths and amplitudes of the input voltage pulses, pressure pulses with various pulse widths and amplitudes can be easily generated using this apparatus. Important characteristics of the pressure pulses such as maximum loading rate (kPa/ms) and total impulse, which is the area under the pressure-time curve, can also be controlled by manipulating input voltage pulse profiles. Molecular dynamics simulations

suggest parameters like peak pressure, pulse duration, maximum loading rate, and total impulse have a significant effect on cell membrane deformation [46]. Thus, having an experimental apparatus that could generate various pressure loadings spanning this parameter space facilitates to experimentally test the numerical findings.

The comparison between the pressure profile generated using a modified SHPB setup [14] and this apparatus is also shown in Fig. 10. The input excitation pulse 2 was designed in such a way that the pressure pulse generated by the apparatus has a similar pulse width and magnitude compared to the pressure waveform obtained from the SHPB experiment. Our apparatus could not only replicate the pressure generation capabilities of an SHPB setup but also exceed them in terms of generating tunable pressure profiles.

At the end of each excitation pulse, the input to the actuator was set to 0 V as shown in Fig. 9(a). Thus, the excitation input to the actuator was stopped, allowing the actuator to discharge. The actuator and the piston were allowed to come to rest on their own. Part of the pressure profiles, since the actuation was stopped, shows

Fig. 9 (a) Sinusoidal excitation pulses given as inputs to the apparatus. (b) Output pressure pulses generated by the apparatus for corresponding input pulses



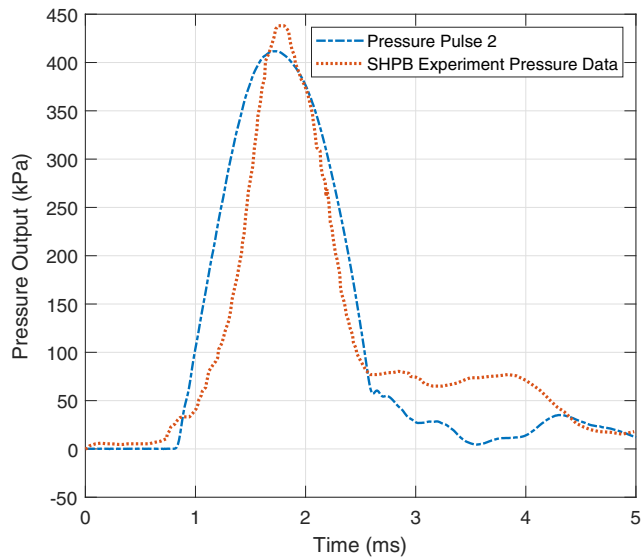


Fig. 10 Comparison between the pressure pulse generated by our apparatus and the pressure profile obtained from SHPB experiment [14]

this transient response of the apparatus and eventually pressure decays to zero as seen in Fig. 9(b). The amplitude of this transient pressure was always found to be less than 10 % percent of the pressure amplitude during the loading cycle.

Friedlander Waveform

A Friedlander waveform consists of an instantaneous rise in pressure followed by an exponential decay and lastly, a negative pressure phase [15]. The time duration for which the pressure is above the atmospheric pressure is known as the positive phase duration of the waveform. As an illustration, a Friedlander waveform having a maximum pressure of 450 kPa and positive phase duration of 10 ms is shown in Fig. 11. In order to generate a Friedlander waveform, the input voltage signal was constructed to have a sharp rise followed by an exponential decay. The negative phase feature of the Friedlander waveform was not incorporated in the input voltage signal because of the actuator limitation that it could only be operated within a 0 – 10 V range to generate compression, not tension. The input voltage signal starts with an instantaneous rise to the top voltage, followed by a hold time of 1 ms, and an exponential decay that lasts 10 ms. This input excitation and the resulting output pressure profiles are shown in Fig. 12. The two pressure profiles were obtained when the same input voltage profile was fed to the actuator. These two pressure profiles replicate each other very closely, confirming the repeatability of the apparatus.

Even though the input excitation can have an instantaneous rise, the response time of the system is finite. The

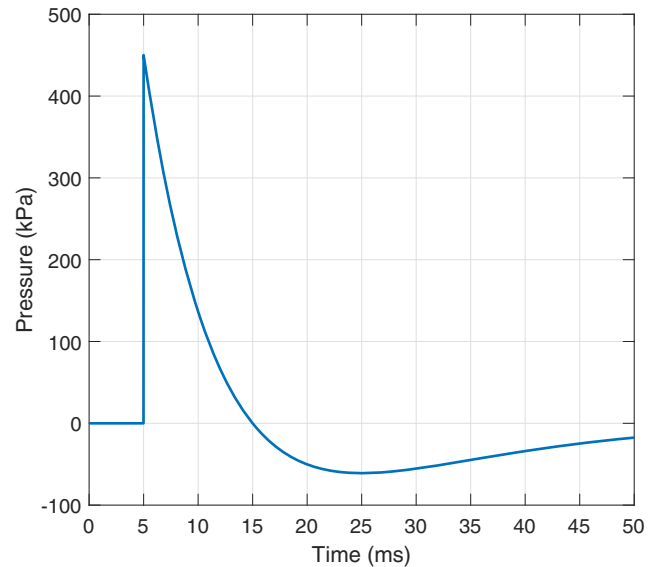


Fig. 11 A Friedlander waveform with 450 kPa maximum pressure and 10 ms positive phase duration

response time of the system depends primarily on the operational frequency-bandwidth of the piezoelectric actuator. If the input pulse had a sharp peak like a Friedlander wave, instead of the flat-top shown in Fig. 12, the system would not have had enough time to respond and would not have generated a pressure peak.

After this initial characterization, we determined that the maximum pressure that could be generated with the current implementation of our apparatus is 450 kPa, which is limited by the geometry of the confinement and the maximum displacement range of the piezoelectric actuator. The maximum operating frequency of this particular actuator

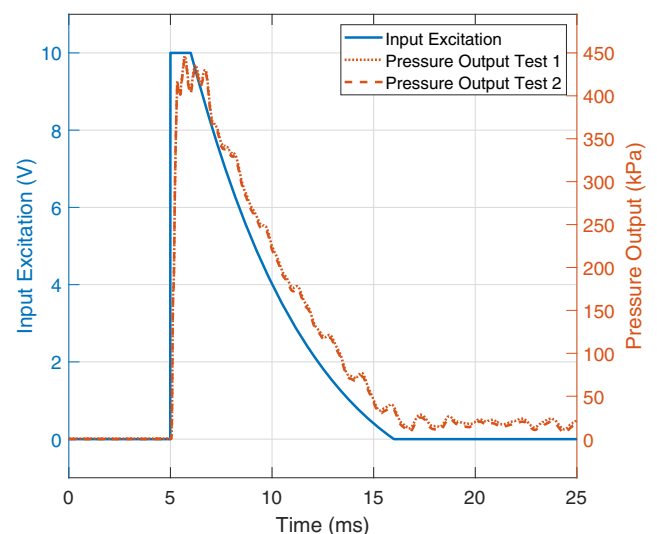


Fig. 12 Comparison between a Friedlander like input excitation waveform given to the apparatus (left y-axis) and the output pressure profiles (right y-axis) generated by the apparatus

Table 4 Sinusoidal components of multi-modal target pressure profile

Frequency (Hz)	Amplitude (kPa)	Phase (rad)	Offset (kPa)
500	75	1.5π	75
1000	75	1.5π	75
2000	75	1.5π	75

is 5 kHz, which also imposes limits to the shortest rise time for pressure generation and high-frequency spectral components of the loading cycle.

Multi-modal Waveform

The implementation of the feedforward controller was demonstrated by solving the output tracking problem for a multi-modal target output profile. As a test case, a multi-modal pressure profile was constructed by adding three sine waves of frequencies 500 Hz, 1000 Hz, and 2000 Hz. The amplitudes and the phases of the sinusoids used to construct the target pressure profile are detailed in Table 4. Also, offsets equal to the amplitudes of sinusoids were added to make the target profile non-negative. The multi-modal target pressure profile constructed for the output tracking problem is shown in Fig. 13.

The designed feedforward controller was used to determine the control input profile. The control input profile generated by the controller for this output tracking problem is shown in Fig. 14. It is noticeable that the control input profile exhibits the amplitude and phase modulation characteristics of the system. This control input profile was then fed to the amplifier that powered the

piezoelectric actuator. The output pressure profile generated by the apparatus in response to the control input profile was recorded. This experiment was repeated twice and the measured pressure profiles for both the experiments are shown in Fig. 15 along with the target pressure profile.

The experimental pressure profiles were found to be in good agreement with the target pressure profile. The two experimental pressure profiles were almost identical, indicating the repeatability of the experimental results. The experimental pressure profiles provided an over 96 % fit to the target pressure profile based on the normalized mean squared error (NMSE) calculation. Thus, this proposed feedforward control strategy can be used to fairly track a complex pressure profile composed of the sinusoids having frequencies between 100 Hz to 5 kHz.

Conclusion

A novel apparatus was designed to generate complex pressure profiles by using a piston-cylinder assembly filled with water. A piezoelectric actuator was used to displace the piston. The displacement of the piston driven by the actuator was controlled through the voltage excitation input given to the actuator. This displaced piston further compressed the water inside the cylinder that generated pressure profiles replicating the dynamics of the input voltage excitation profiles. To test the capabilities of the apparatus, the piezoelectric actuator was excited with various input voltage profiles that included single sinusoidal pulses and a Friedlander-like waveform. The pressure profiles obtained for these input excitation profiles followed the temporal and magnitude characteristics of their respective input

Fig. 13 Multi-modal target pressure profile constructed for an output tracking problem

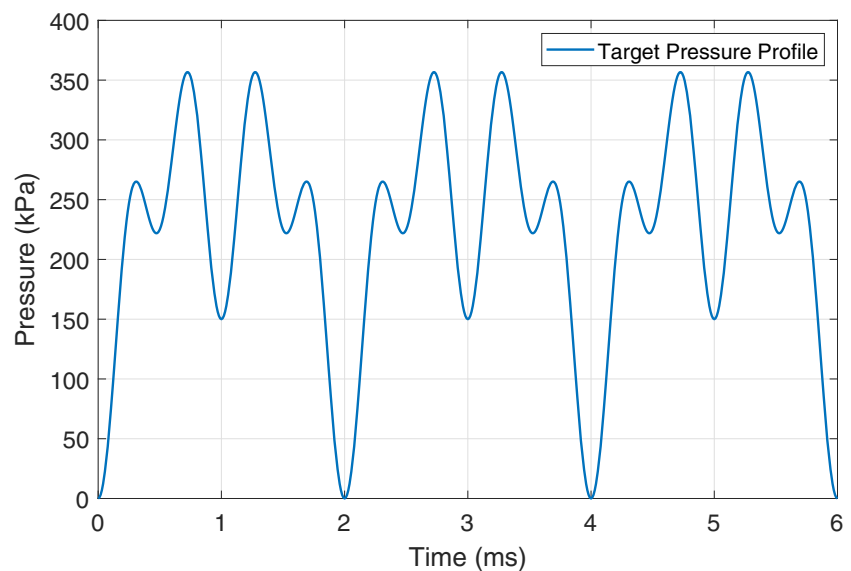
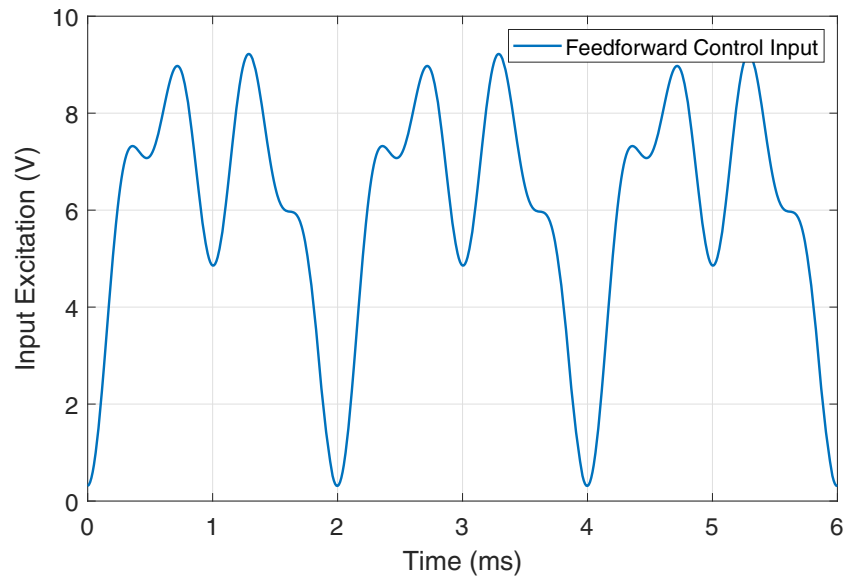


Fig. 14 Control input profile determined by the feedforward controller

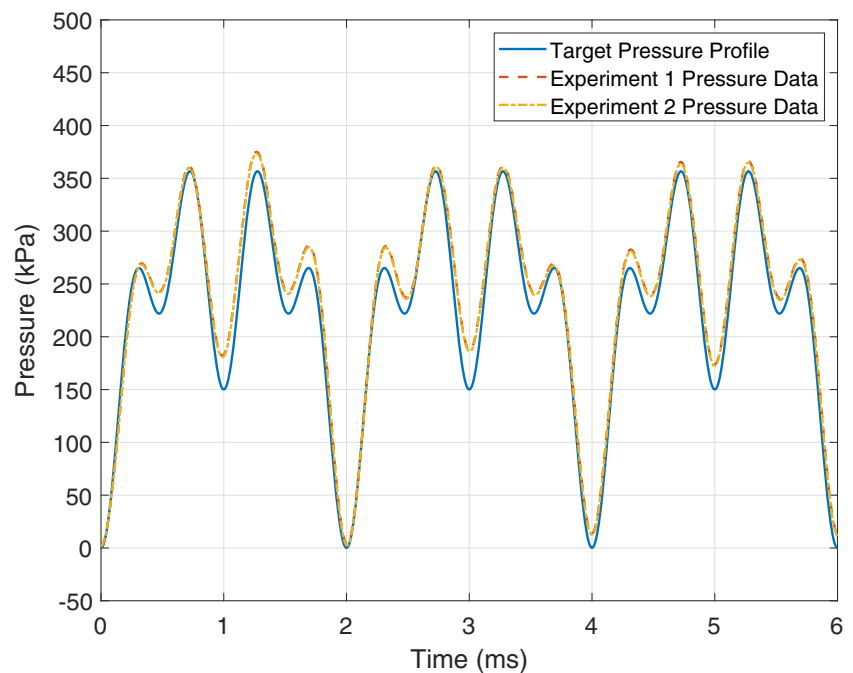


profile. Moreover, a feedforward controller was designed and implemented, which enabled the apparatus to generate complex user-defined pressure profiles.

Split-Hopkinson Pressure Bars, shock-tubes, and blast-tubes are relatively complex systems with inherent hazards such as high pressure, shock, impact, and loud noise. In consequence, their safe operation requires rigorous technical training. Also, they lack portability due to their typically large footprint ($\sim 10 \text{ m}^2$ or more) and anchoring requirements (e.g., vibration isolation); and are in general

not tunable in the sense that their ability to produce arbitrary loading cycles is very limited. Our apparatus overcomes all of these limitations due to its very small footprint ($\sim 4 \times 10^{-2} \text{ m}^2$), no special anchoring requirements, no inherent safety concerns, technical simplicity, and its ability to produce virtually any arbitrary loading cycle within its pressure and frequency bounds. In addition, our apparatus fits inside any fume hood due to its compactness, increasing its suitability for biomedical applications. Depending on the choice of piezoelectric actuator, an apparatus like the

Fig. 15 Comparison between the target pressure profile and the experimental pressure profiles obtained using the feedforward controller



one presented herein is suitable for applications that require resonant frequencies in the range 5 kHz – 16 kHz, and peak pressures of up to 450 kPa.

Typical *ex-vivo* and *in-vitro* experiments on living tissue, organoids, or cell cultures are performed in nearly incompressible media such as artificial cerebrospinal fluid or other aqueous solutions [13, 14, 23, 47], enabling our apparatus for studies of the effect of dynamical loading on these kinds of biological systems.

The inner diameter of the tube is based on the diameter of the piezoelectric actuator (11.2 mm). Its inner volume was optimized for the operational characteristics of the piezo actuator. In principle, the inner diameter of the confinement could be increased, but it would require some additional design optimization beyond just a change in scale to offer similar operational characteristics as with the basic design. The same idea goes for any attempt to increase the maximum pressure, or the maximum achievable frequency: the resonant frequency, stroke, and maximum force of the piezo actuator define the limitations to each new design.

The current implementation of this apparatus does not include volumetric expansion of the confinement chamber, limiting its operation to positive gauge pressures. With the intention to expand our studies to the effect of cavitation [10–12, 24, 25], future implementations will include the ability of exerting volumetric expansions.

Acknowledgements This work was sponsored in part by Michigan State University and in part by the Air Force Research Laboratory (award No. FA8650-18-2-6880).

The view(s) expressed herein are those of the author(s) and do not reflect the official policy or position of Brooke Army Medical Center, the U.S. Army Medical Department, the U.S. Army Office of the Surgeon General, the Department of the Army, the Department of the Air Force, the Department of Defense, or the U.S. Government.

Declarations

Competing interests On behalf of all authors, the corresponding author states that there is no conflict of interest.

References

- Fischer H (2013) Us military casualty statistics: operation new dawn, operation iraqi freedom, and operation enduring freedom. Library of Congress Washington Dc Congressional Research service
- Meaney DF, Morrison B, Bass CD (2014) The mechanics of traumatic brain injury: a review of what we know and what we need to know for reducing its societal burden. *J Biomech Eng* 136(2):021008
- Bass CR, Panzer MB, Rafaels KA, Wood G, Shridharani J, Capehart B (2012) Brain injuries from blast. *Ann Biomed Eng* 40(1):185–202
- Chen YC, Smith DH, Meaney DF (2009) In-vitro approaches for studying blast-induced traumatic brain injury. *J Neurotrauma* 26(6):861–876
- Nakagawa A, Manley GT, Gean AD, Ohtani K, Armonda R, Tsukamoto A, Yamamoto H, Takayama K, Tominaga T (2011) Mechanisms of primary blast-induced traumatic brain injury: insights from shock-wave research. *J Neurotrauma* 28(6):1101–1119
- Lew HL (2005) Rehabilitation needs of an increasing population of patients: Traumatic brain injury, polytrauma, and blast-related injuries. *J Rehabil Res Dev* 42(4):xiii
- Scott SG, Belanger HG, Vanderploeg RD, Massengale J, Scholten J (2006) Mechanism-of-injury approach to evaluating patients with blast-related polytrauma. *J Am Osteopath Assoc* 106(5):265
- Taber KH, Warden DL, Hurley RA (2006) Blast-related traumatic brain injury: what is known? *J Neuropsych Clin Neurosciences* 18(2):141–145
- Sosa MAG, De Gasperi R, Paulino AJ, Pricop PE, Shaughnessy MC, Maudlin-Jeronimo E, Hall AA, Janssen WGM, Yuk FJ, Dorr NP et al (2013) Blast overpressure induces shear-related injuries in the brain of rats exposed to a mild traumatic brain injury. *Acta Neuropathologica Commun* 1(1):51
- Taylor PA, Ludwigsen JS, Ford CC (2014) Investigation of blast-induced traumatic brain injury. *Brain Injury* 28(7):879–895
- Hong Y, Sarntinoranont M, Subhash G, Canchi S, King MA (2016) Localized tissue surrogate deformation due to controlled single bubble cavitation. *Exp Mech* 56(1):97–109
- Bustamante MC, Singh D, Cronin DS (2018) Polymeric hopkinson bar-confinement chamber apparatus to evaluate fluid cavitation. *Exp Mech* 58(1):55–74
- Sarntinoranont M, Lee SJ, Hong Y, King MA, Subhash G, Kwon J, Moore DF (2012) High-strain-rate brain injury model using submerged acute rat brain tissue slices. *J Neurotrauma* 29(2):418–429
- Canchi S, Sarntinoranont M, Hong Y, Flint JJ, Subhash G, King MA (2017) Simulated blast overpressure induces specific astrocyte injury in an ex vivo brain slice model. *PLoS one* 12(4):e0175396
- Dewey JM (2010) The shape of the blast wave: studies of the friedlander equation. In: *Proceeding of the 21st International Symposium on Military Aspects of Blast and Shock (MABS)*, Israel, pp 1–9
- Chandra N, Ganpule S, Kleinschmit NN, Feng R, Holmberg AD, Sundaramurthy A, Selvan V, Alai A (2012) Evolution of blast wave profiles in simulated air blasts: experiment and computational modeling. *Shock Waves* 22(5):403–415
- Tan XG, Przekwas AJ, Gupta RK (2017) Computational modeling of blast wave interaction with a human body and assessment of traumatic brain injury. *Shock Waves* 27(6):889–904
- Przekwas A, Garimella HT, Tan XG, Chen ZJ, Miao Y, Harrant V, Kraft RH, Gupta RK (2019) Biomechanics of blast tbi with time-resolved consecutive primary, secondary, and tertiary loads. *Military Med* 184(Supplement_1):195–205
- Fievisohn E, Bailey Z, Guettler A, VandeVord P (2018) Primary blast brain injury mechanisms: current knowledge, limitations, and future directions. *J Biomech Eng* 140(2):020806
- Bolander R, Mathie B, Bir C, Ritzel D, VandeVord P (2011) Skull flexure as a contributing factor in the mechanism of injury in the rat when exposed to a shock wave. *Ann Biomed Eng* 39(10):2550
- Moss WC, King MJ, Blackman EG (2009) Skull flexure from blast waves: a mechanism for brain injury with implications for helmet design. *Phys Rev Lett* 103(10):108702
- Chen WW, Song B (2010) Split hopkinson (kolsky) bar: design, testing and applications. Springer Science & Business Media



23. Nienaber M, Lee JS, Feng R, Lim JY (2011) Impulsive pressurization of neuronal cells for traumatic brain injury study. *JoVE (J Vis Exper)* (56):e2723
24. Goeller J, Wardlaw A, Treichler D, O'Bruba J, Weiss G (2012) Investigation of cavitation as a possible damage mechanism in blast-induced traumatic brain injury. *J Neurotrauma* 29(10):1970–1981
25. Salzar RS, Treichler D, Wardlaw A, Weiss G, Goeller J (2017) Experimental investigation of cavitation as a possible damage mechanism in blast-induced traumatic brain injury in post-mortem human subject heads. *J Neurotrauma* 34(8):1589–1602
26. Panzer MB, Matthews KA, Yu AW, Morrison B, Meaney DF, Bass CR (2012) A multiscale approach to blast neurotrauma modeling: part i—development of novel test devices for in vivo and in vitro blast injury models. *Front Neurol* 3:46
27. Effgen GB, Hue CD, Vogel III E, Panzer MB, Meaney DF, Bass C, Morrison III B (2012) A multiscale approach to blast neurotrauma modeling: part ii: methodology for inducing blast injury to in vitro models. *Front Neurol* 3:23
28. Needham CE, Ritzel D, Rule GT, Wiri S, Young L (2015) Blast testing issues and tbi: experimental models that lead to wrong conclusions. *Front Neurol* 6:72
29. Logan NJ, Arora H, Higgins CA (2017) Evaluating primary blast effects in vitro. *JoVE (J Vis Exper)* (127):e55618
30. Campos-Pires R, Yonis A, Macdonald W, Harris K, Edge CJ, Mahoney PF, Dickinson R (2018) A novel in vitro model of blast traumatic brain injury. *JoVE (J Vis Exper)* (142):e58400
31. Bauman RA, Ling G, Tong L, Januszkiewicz A, Agoston D, Delanerolle N, Kim Y, Ritzel D, Bell R, Ecklund J et al (2009) An introductory characterization of a combat-casualty-care relevant swine model of closed head injury resulting from exposure to explosive blast. *J Neurotrauma* 26(6):841–860
32. Alley MD, Schimizze BR, Son SF (2011) Experimental modeling of explosive blast-related traumatic brain injuries. *Neuroimage* 54:S45–S54
33. De Lanerolle NC, Bandak F, Kang D, Li AY, Du F, Swauger P, Parks S, Ling G, Kim JH (2011) Characteristics of an explosive blast-induced brain injury in an experimental model. *J Neuropathol Exper Neurol* 70(11):1046–1057
34. Risling M, Plantman S, Angeria M, Rostami E, Bellander B-M, Kirkegaard M, Arborelius U, Davidsson J (2011) Mechanisms of blast induced brain injuries, experimental studies in rats. *Neuroimage* 54:S89–S97
35. Nakagawa A, Fujimura M, Kato K, Okuyama H, Hashimoto T, Takayama K, Tominaga T (2008) Shock wave-induced brain injury in rat: novel traumatic brain injury animal model. In: *Acta Neurochirurgica Supplements*. Springer, pp 421–424
36. Zander NE, Piehler T, Banton R, Benjamin R (2017) Bioeffects on an in vitro model by small-scale explosives and shock wave overpressure impacts. Technical Report, US Army Research Laboratory Aberdeen Proving Ground United States
37. Engineering Toolbox: Bulk Modulus and Fluid Elasticity. <https://www.engineeringtoolbox.com/>
38. Williams PR, Williams PM, Brown SWJ (1998) Cavitation phenomena in water involving the reflection of ultrasound pulses from a free surface, or from flexible membranes. *Phys Med Biol* 43(10):3101
39. Sadd MH (2009) Elasticity: theory, applications, and numerics. Academic Press
40. Bedford AM, Drumheller DS (1994) Introduction to elastic wave propagation. Wiley
41. Kolsky H (1963) Stress waves in solids. Dover Books on Physics. Dover Publications
42. Graff KF (1991) Wave motion in elastic solids. Dover Books on Physics Series. Dover Publications
43. Meyers MA (1994) Dynamic behavior of materials. Wiley-Interscience publication. Wiley
44. Khalil HK (2002) Nonlinear systems. Upper Saddle River
45. Antsaklis PJ, Michel AN (2006) Linear systems. Springer Science & Business Media
46. Kfoury R, Marzban B, Makki E, Greenfield ML, Yuan H (2019) Effect of pressure profile of shock waves on lipid membrane deformation. *PloS one* 14(2):e0212566
47. Koo B, Choi B, Park H, Yoon K-J (2019) Past, Present, and Future of Brain Organoid Technology. *Mol Cells* 42(9):617

Publisher's Note Springer Nature remains neutral with regard to jurisdictional claims in published maps and institutional affiliations.

